MASTER OF PHILOSOPHY

Novel Schemes for the Collimation of Neutral Electron-Positron Beams

Bailie, David

Award date:
2016

Awarding institution:
Queen's University Belfast

Queen's University Belfast

School of Mathematics and Physics

MSci Thesis

Novel Schemes for the Collimation of Neutral Electron-Positron Beams

---

Author:
David Bailie

Supervisor:
Dr. Gianluca Sarri

19 February, 2016

Abstract

Electron-Positron beams represent a unique state of matter that present overall charge neutrality and therefore not embedded by self-generated magnetic fields. These beams are believed to be emitted as highly collimated astronomical jets by some of the most powerful and distant astrophysical objects in the Universe such as Black-holes, pulsars, and quasars. Theory suggests that as these beams propagate through space instabilities occur between the electrons and positrons as they interact with the interstellar medium. This causes the electrons and positrons to filament out into separate beam-lets that set up strong magnetic fields between them. What drives the micro-physics behind such phenomena is still a mystery and an on going area of research. To gain a deeper understanding of how these neutral pair plasmas are formed and their dynamics, a small scale reproduction in the laboratory would open the doors for a new field of research into the world of laboratory astrophysics.

Despite the intrinsic difficulty in reproducing neutral pair plasmas in the laboratory, recent experiments carried out using a laser driven set-up have for the first time created a neutral ion free electron-positron plasma, with high-density and divergence on the order of 20 mrad. However, although small this divergence leads to the beam quickly losing density, so that within the first few mm any collective behaviour in the plasma is lost. For a meaningful study of the dynamics of electron-positron beams in the laboratory, it is necessary that these beams be kept highly collimated. Numerical simulations indicate that an electron beam with a converging full-cone angle of 20 mrad incident onto a lead target, initiates an electrodynamic cascade that produces a highly collimated neutral electron-positron beam. Here, through analytical and numerical analysis we show that the electron beam can be converged onto the target by using a system comprising of three miniature magnetic quadrupoles, along with obtaining the parameters for these quadrupoles.

Contents

1 Introduction

1.1 Astrophysical Pair Plasmas

Electron-Positron beams are believed to be emitted as highly collimated jets and ultra-relativistic winds by some of the most energetic and distant (hence oldest) astrophysical objects in the Universe such as black-holes [1, 2], active galaxies (i.e. quasars, radio galaxies) [3, 4] and pulsars [5, 6].

It is still an ongoing area of research to understand how exactly collimated astrophysical jets are formed and what powers them, although it is commonly believed that in most cases they originate from a central compact object that is surrounded by a magnetised accretion disk. As the accretion disk is moving around the dense core it is thought to lose angular momentum causing material to fall into the core. Due to tangled magnetic fields between the core and the accretion disk, particles from this material are collimated into jets that point up and down and away from the core, these jets are then projected outwards with very high velocities (sometimes relativistic) and perpendicular to the plane of the accretion disk [1, 2, 7]. Likewise the composition of these jets are still an open area of debate within the scientific community. Some studies favour that jets stemming from the accretion disk consist of electrons and positive ions, whilst an increasing number of studies argue that they are made up of electrons and positrons, which are produced in pair cascades in the intense fields near the surface of the dense core [3, 8].

Theory suggests that as these electron-positron beams are projected into space, due to the symmetry between them (same mass, absolute charge) they initially represent a unique state of matter that have an overall charge neutrality and thus not embedded by self-generated magnetic fields. As they continue to propagate onwards it is believed that instabilities occur between the electrons and positrons as they interact with the interstellar medium and collisionless shocks are generated via collective excitations [9, 10] in the plasma. This causes the electrons and positrons to filament out into separate beam-lets that set up strong magnetic fields between them. The kinetic energy of the particles in the beam goes into producing these magnetic fields, until a point of equipartition is reached, resulting in the beam slowing down (see section on Current Filamentation Instability). As the positrons and electrons spiral about these field lines (in opposite directions) they release non thermal radiation in the form of gamma rays tangentially outwards, this is due to

synchrotron radiation since the particles are constantly accelerating [11, 12, 13]. These strong magnetic fields are consistent with evidence of the magnetic fields in the direction of such phenomenon being much stronger than the background magnetic fields of the Universe [14], which can be deduced from the strong gamma rays reaching Earth from astrophysical jets that travel perpendicular to the line of sight. These gamma rays are also evidence for the jets consisting of a neutral pair plasma of electron-positrons, due to observations of some of these jets being optical thin [3, 15].

If it where possible to probe the aforementioned phenomena then it would test physics at its absolute limits, whilst providing a glimpse into the very early Universe. Unfortunately the distances are much too great and their indirect radiative signatures along with matching numerical models have to be relied upon [12].

To gain a deeper understanding of how these neutral pair plasmas are formed and their dynamics, a small scale reproduction in the laboratory would open the doors for a new field of research into the world of laboratory astrophysics. Besides this, the fundamental interest to plasma science in creating such a state of matter is expected to produce new results on wave and turbulence dynamics due to the mass and charge symmetry between the positive and negative particles [16].

1.2 The First Experimental Generation of a Neutral Electron-Positron Beam in the Laboratory

Scaling down these astrophysical sized phenomena to that on the scale of plasmas created in the laboratory, would allow for the study of the processes that go into causing filamentation of the neutral beam that leads to the generation of such strong magnetic fields. This would help with validating the numerical models that are created to interpret these astrophysical observations. The problem in doing so is the intrinsic difficulty in creating electron-positron plasmas in the laboratory that can be studied. This has been widely attempted across the scientific community, but without any success, even evading some of the largest particle accelerators such as CERN. Some of these experiments have shown positive results in producing electron-positron beams, mainly by the generation of separate electron and positron populations and then recombining them [17, 18]. Whilst other experiments have avoided this problem of recombination by producing pair plasmas together from the

same source [19, 20, 21]. Although due to a low percentage of positrons compared to electrons ($< 10\%$) and producing beams of low density, this does not allow for a neutral beam with plasma like behaviour, which is essential to the study of this state of matter.

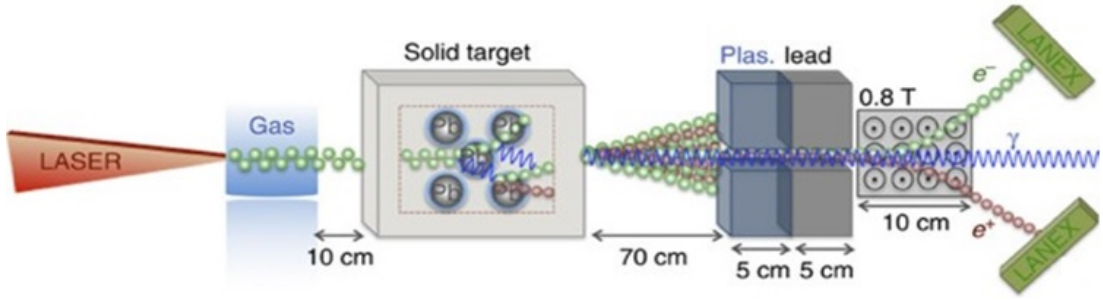

Figure 1: Laser accelerated electrons (green spheres) moving at relativistic speeds are impacted onto a solid lead target. This initiates a quantum electrodynamic cascade consisting of electrons, positrons (red spheres), and photons (blue sinusoids). The escaping electrons and positrons from the rear of the lead target are separated out and resolved by a magnetic spectrometer and a pair of LANEX screens. The magnetic spectrometer consists of an entrance diameter of $\sim$ 15 mm, with 5 cm plastic followed by 5 cm of lead shielding. This helped to shield the detector from noise generated by low energy electrons and gamma-rays generated, at wide angles, when the laser interacted with the gas and the electrons impacted onto the lead target. Image adapted from Ref. [22].

That is until recently, using the fully optical and compact ASTRA-GEMINI laser system at the Rutherford Appleton Laboratory (RAL), the first experimental generation of a high density ($n_e \sim 10^{15} - 10^{16}$ cm^{-3}, allowing for collective effects to occur), narrow divergence ($\theta_{e+} \sim$ 10-20 mrad) and neutral electron-positron beam in the laboratory was carried out [22], led by a research group from Queens University Belfast. This was achieved using a compact laser driven setup (shown schematically in Fig.1), where a high powered laser was focussed onto a supersonic He gas jet doped with 3.5% of N_2. This interaction produced an electron beam with a maximum energy order of 600MeV and a full width half maximum divergence of 2 mrad. This electron beam was then directed onto a lead solid target of different thicknesses that covered multiples of the material's radiation length (d=0.5, 1, 1.5, 2, 2.5, 3, and 4

cm, given that the radiation length for lead is $L_{rad} \approx 0.5$ cm), initiating a quantum electrodynamic cascade involving electrons, positrons and photons. The escaping electrons and positrons from the rear of the lead target where then separated and spectrally resolved by a magnetic spectrometer and a pair of LANEX screens.

The results from this experiment can be seen in the three graphs shown in Fig.2 (blue circles), which depict the measured number of electrons and positrons at the exit of the lead target as a function of thickness (d). Plot a shows how the yield of positrons has its maximum at d=1 cm which is equivalent to two radiation lengths of lead, while plot b shows how the number of electrons exiting the target as a function of thickness decreases, due to the increasing number of positrons being created in the electro-dynamic cascade. More interestingly plot c shows the total positron fraction in the leptonic beam as a function of the lead thickness. As the thickness is increased there comes a point around the d=2.5 cm mark (corresponding to five radiation lengths of lead) where the ratio of positrons accounts for approximately 50% of the leptonic beam. This percentage is preserved as the target thickness continues to increase although a target thickness of d=2.5 cm yields the highest density of the neutral electron-positron beam. This is due to maximum energy gradually decreasing because of an increased probability of energy loss as the particles propagate through the thicker target, hence allowing less particles to escape the lead. These plots also show that the experimental values match well to numerical (red crosses in Fig.2) and analytical models (dashed green lines in Fig.2).

The results of this experiment now pave the way for reproducing in the laboratory some of the astronomical phenomenon as previously discussed.

1.3 Current Filamentation Instability

As previously mentioned in section 1.1, instabilities occur between the electrons and positrons as they interact with the interstellar medium and collisionless shocks are formed. Collisionless shocks require collective behaviour in the plasma in order to generate plasma waves, and it is believed that strong electric and magnetic fields are necessary to produce such collective behaviour [9, 10]. In a leptonic jet that initially has an overall charge neutrality and thus not embedded by self-generating magnetic fields, it is postulated that these strong fields are produced by the filamentation of the particles into beam-lets due to instabilities occurring on interacting with the

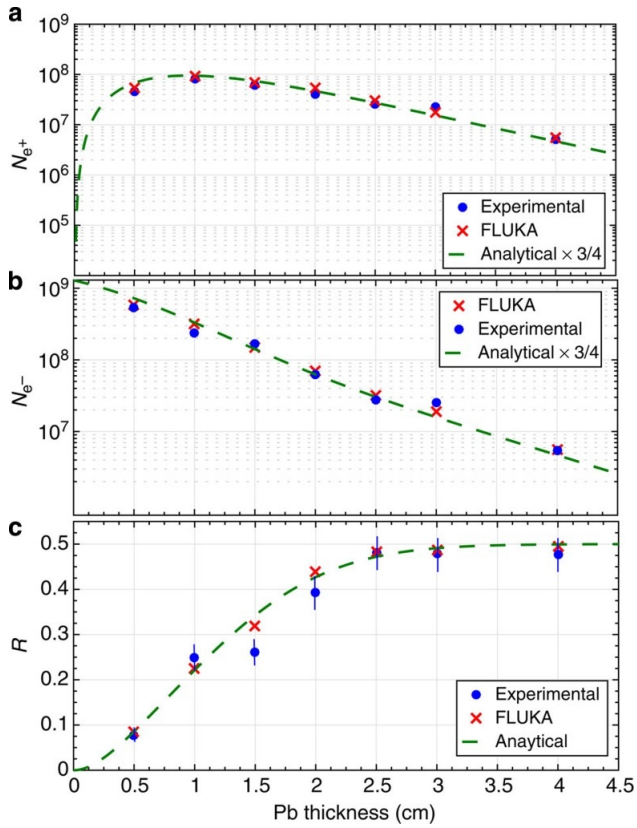

Figure 2: (a) Measured number of positrons (blue circles) as a function of the target thickness. (b) Measured number of electrons (blue circles) as a function of the target thickness. For these two frames, error bars lie within the size of the circles. (c) Measured total positron fraction (blue circles) in the leptonic beam as a function of the target thickness. For all frames, the green dashed line represents the analytical prediction and the red crosses represent the numerical simulation. Also for all three frames, the error bars mainly arise from shot-to-shot fluctuations. Image adapted from Ref. [22].

interstellar medium [11, 12, 13]. The strength of theses magnetic fields is defined by a dimensionless parameter known as the energy density ratio $\varepsilon_B = U_B/U_e$, where $U_B = B^2/2\mu_0$ is the magnetic energy density and $U_e = n_e\gamma m_e c^2$ is the beam energy density. Observations of the gamma rays produced by such astrophysical phenomena indicate that the value of ε_B ranges between 10^{-5} [23, 24] and 10^{-1} [25, 26]. There are other mechanisms that can generate magnetic fields in collisionless shocks but these are either too small ($\varepsilon_B \sim 10^{-9}$) such as, compressional amplification of the

weak pre-existing magnetic field in the interstellar medium [27] or, the field decays rapidly such as the transverse Weibel instability [28].

In place of the interstellar electron-ion plasma a low density gas can be inserted into the target chamber of an experimental set-up similar to that in Fig.1. This would allow for the study of the dynamics of a neutral beam as it propagates through this gas. 3-D Particle-In-Cell (PIC) simulations such as the one in Fig.3 [29] show that instabilities in a highly collimated, neutral electron-positron beam can arise upon interacting with this gas and strong current filamentation can develop. This is in contrast to simulations of a purely electronic beam that does not show any filamentation occurring.[22]

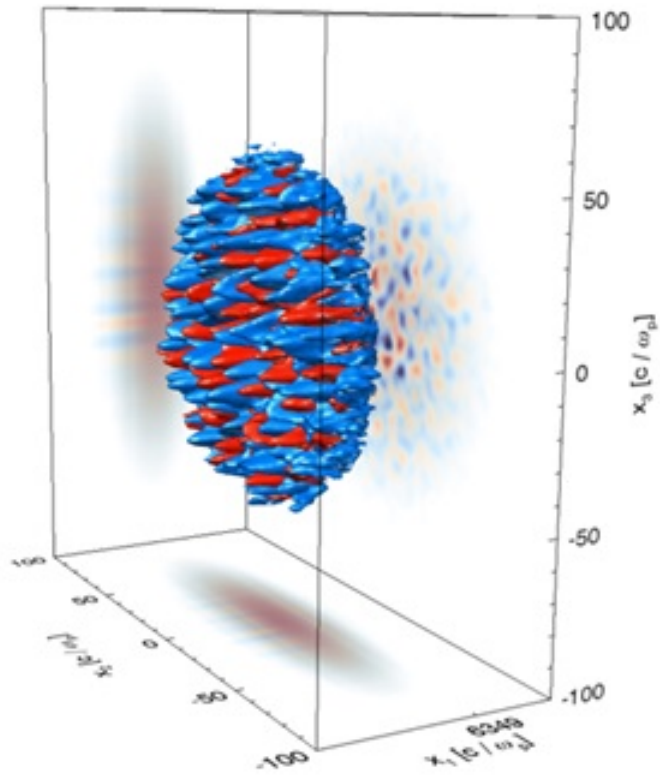

Figure 3: 3-D particle-in-cell simulation for the propagation of a highly collimated, neutral electron-positron beam through a background electron-ion plasma, shows that current filamentation instabilities could develop. Electron beam-lets represented in blue and positron beam-lets represented in red. Image from Ref. [29].

As the filamentation of the neutral plasma grows with distance then so to does the strength of the magnetic field which can be seen from the graph in Fig.4 [29]. This shows the magnetic field strength ranging with an ε_B value $\varepsilon_B = 10^{-4}$ (similar to observations of astrophysical jets, which range between $10^{-5} < \varepsilon_B < 10^{-1}$) in the early stages of filamentation up to a saturation point (almost complete equipartition) around the 20 mm mark. At this point most of the kinetic energy of the jet has been put into producing the strong magnetic field and the particles of the jet are slowed down asymptotically.

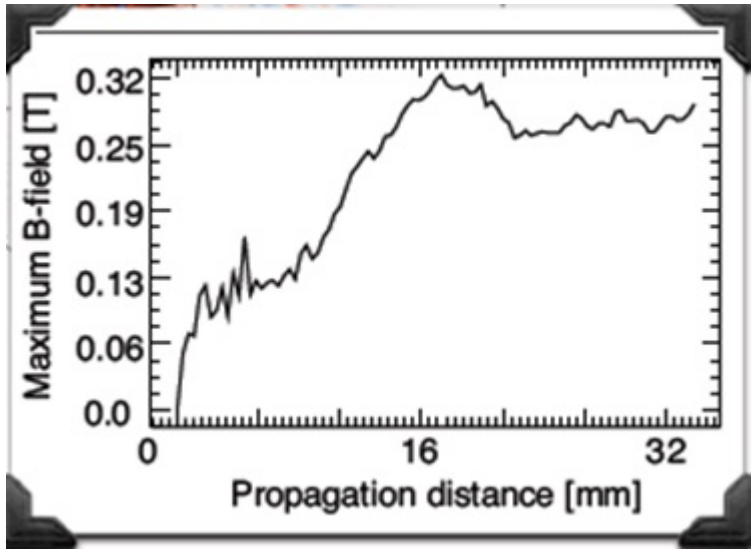

Figure 4: Magnetic field strength increasing with current filamentation in a highly collimated neutral beam as it propagates through a background electron-ion plasma. Saturation occurs around the 20 mm mark. Image from Ref. [29].

In another experiment carried out by the same research group from Queen's University Belfast, this principle of a gas inserted into the target chamber was tested using the Gemini laser. In brief, the newly created neutral electron-positron beam was made to propagate through a gas-cell filled with helium, which was then transversely probed using a proton imaging technique [30]. If filamentation occurred then it was expected that a LANEX screen would display a modulated distribution, resulting from a high-intensity gamma-ray beam. The results are confirmed by proton radiographs taken of the background plasma (see Fig.5). Frame *a* shows that a purely electronic beam carves out a well collimated channel in the background plasma, while frame *b* shows that a non-neutral electron-positron beam does not

visibly produce any filamentation. Finally frame *c* shows two lobes believed to be produced by an accumulation of protons being deflected in a magnetic field due to filamentation of the neutral electron-positron beam as it passes through the low density gas. These results indicate that filamentation only occurs for neutral pair plasmas, in accordance with theoretical predictions [22].

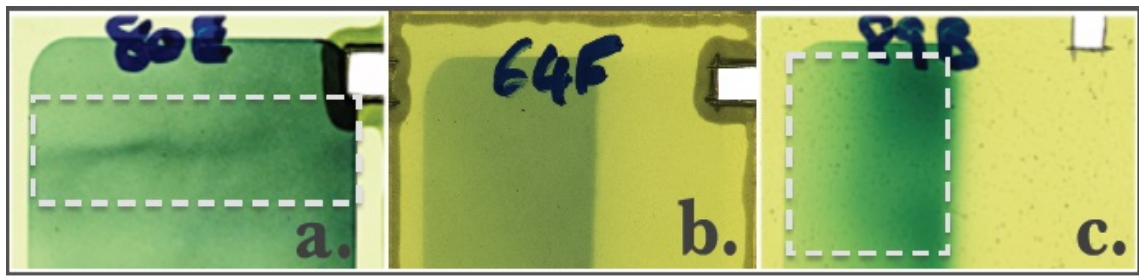

Figure 5: Evidence of the magnetic fields produced in the background plasma onto proton radiographs. (a) Radiograph for a purely electronic beam with no lead target inserted. (b) Radiograph for a non-neutral electron-positron beam, consisting of 30% positrons. Shows no modulation of the probing proton beam. (c) Radiograph for a neutral electron-positron beam, consisting of 47% positrons. Shows a clear modulation of the probing proton beam. Each frame shows the beams propagating from the right-hand side to the left. Image adapted from Ref. [31].

The problem with this experiment is that the electron-positron beams that have been created thus far exit the target with a divergence on the order of 20 mrad leading to the beam rapidly losing density and placing a limit on the analysis of the data obtained. This means that the plasma could only be studied within the first few mm and after that any collective behaviour and the ability to study saturation of instabilities in the plasma is lost.

For a meaningful study of the dynamics of electron-positron beams in the laboratory, it is necessary that these beams be kept highly collimated.

2 Collimating the Electron-Positron Beam

2.1 FLUKA Simulations

The aim of this study is to use magnetic fields in order to achieve a collimated beam. Since the beam needs to remain neutral and initially leave the target with no

instabilities (hence no magnetic fields) using magnetic fields to collimate the electron-positron beam after the target would be impossible, since this would separate out the charges into opposite directions. Instead it has been proposed to use a converging electron beam placed before the lead target in order to initiate the electromagnetic cascade in the solid. The angle of convergence of the electron beam has to be carefully chosen in order to balance the angular spreading of the cascade, thus we require an electron beam with a converging angle of the order of -20 mrad [32].

To show if a converging electron beam incident onto a lead target is a viable method of generating a collimated electron-positron beam, simulations using the Monte-Carlo scattering code FLUKA were carried out (see Fig.6)[31]. This accounts for electromagnetic cascades initiated by an electron beam as it passes through a solid target. Frames a, b and c show the simulated spatial distribution of electrons, positrons and the resulting ratio respectively per primary particle. Each of these frames are in a base 10 logarithmic colour scale which clearly shows that the converging electron beam does produce a collimated cascade within the lead target seen in all three frames from 0 to 2.5 cm. By placing a collimating lead shielding of a few cm directly after the exit of the lead target, this cleans up any off axis particles, leaving the highly collimated electron-positron beams seen in the linear scale frames d, e and f. These beams will have a transverse size that matches that of the collimator, which can be changed to suit the specific requirements of the experiment. Frame g shows by the time the cascade exits the lead target (at 2.5 cm) the positrons account for $\sim 43\%$ of the neutral beam (this slight imbalance does not affect the plasma dynamics, and can be considered neutral. See Ref. [22]), this is preserved up to the end of the simulation.

2.2 Quadrupole Triplet

To achieve a converging electron beam a system comprising of three miniature quadrupoles will be used, which are now available for magnetic fields of the order of 1.2 T [33]. These consist of four opposite poles adjacent to each other (which can be approximated by hyperbolic faced steps or circles), with another eight segments used to close the outer fields (see Fig.7). A quadrupole is a lens that focuses in one axis and defocuses in the other axis and an optical system usually consists of two or more quadrupoles. The advantage of using a triplet system is that the overall

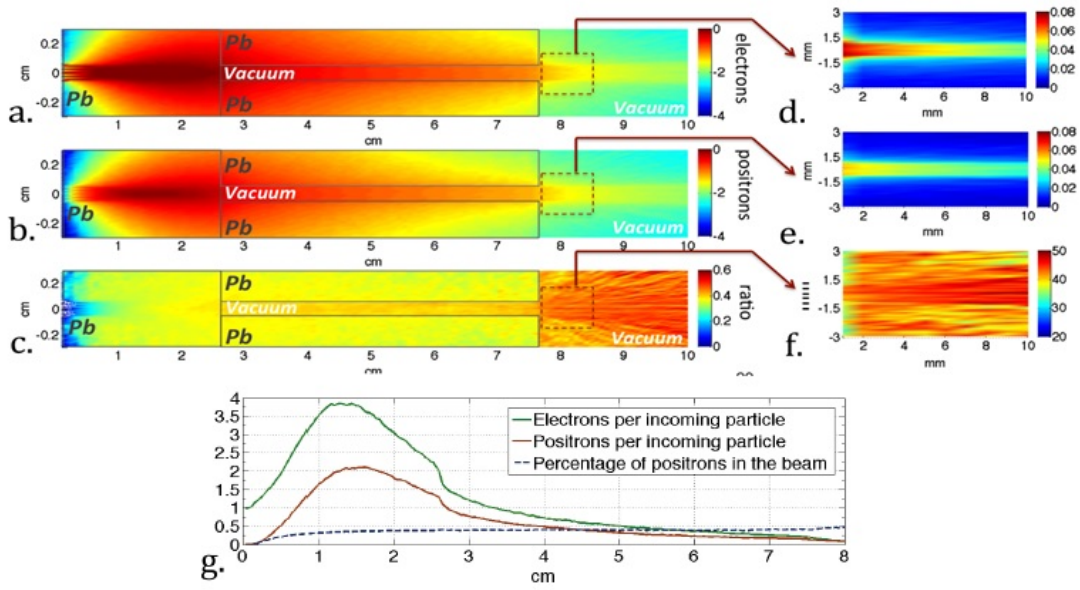

Figure 6: FLUKA simulations showing the feasibility of generating collimated electron-positron beams from an incident converging electron beam. (a),(b) and (c) show the simulated spatial distribution of electrons, positrons and the resulting ratio respectively. The gray rectangle depict the position of the lead target. Frames (d), (e) and (f) show the same quantities, highly collimated, at the exit of the collimator (red dashed rectangles) but in a linear scale. (g) Number of electrons (green solid line) and positrons (brown solid line) per primary particle and the ratio of positrons in the beam (blue dashed line), accounting for $\sim 43\%$ right at the exit of the target.Image adapted from Ref. [31].

beam usually stays rounder and that it offers point to point focusing. If this happens in the x and y axis simultaneously then we refer to this as a stigmatic focusing system for which one point of the object corresponds to one point of the image.The advantage of a triplet system over a doublet is that the lateral magnification in the x and y axis can be made equal [34].

Focusing ions through quadrupoles have been widely used for a long time now and throughout here the classic text book Ref. [34] is referred to.

How particles move through a quadrupole depends on the magnetic flux density $B(x, y, z)$ between the poles, relevant to the optic axis. If the particles travel in the z direction then the scalar magnetic potential is given by

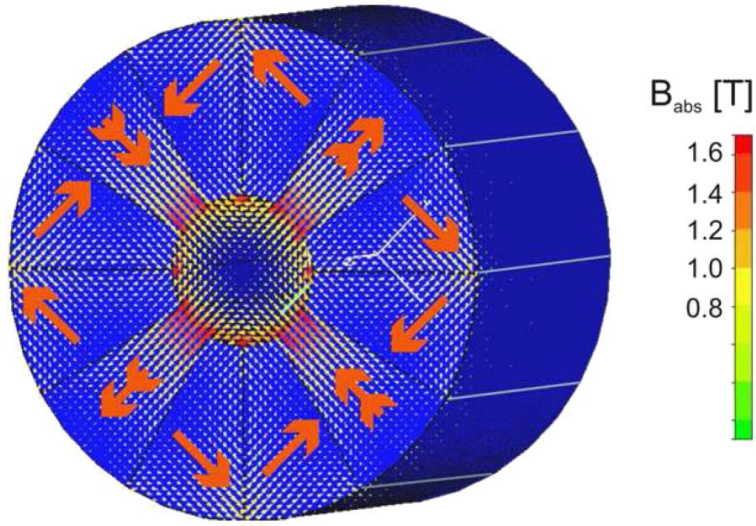

Figure 7: Coloured schematic view of a miniature magnetic quadrupole, available for magnetic fields of the order of 1.2 T. Twelve segments are shown, four of which are opposite poles adjacent to each other (pointing radially) and another eight segments used to close the outer field. The arrows show the direction of magnetization, while the colour indicates the strength of the magnetic field. Here the tip strength is ∼1.5 T. Image taken from Ref.[33].

$$V(x,y) = \frac{2V_0 xy}{G_0^2} = gxy \ , \tag{1}$$

where V_0 is the scalar magnetic potential at the tip of the poles, G_0 is half the aperture width and $g = 2V_0/G_0^2$. Since $B = -\nabla V$, the components of the magnetic flux density B are

$$B_x(x,y) = \frac{\partial V}{\partial x} = -gy \ , \tag{2}$$

$$B_y(x,y) = \frac{\partial V}{\partial y} = -gx \ , \tag{3}$$

showing that the magnetic flux density increases linearly along x and y. From the geometry of the cross section through the pole faces, the pole tips are $x_0 = \pm y_0 = \pm G_0/2$, and the maximum magnetic flux density at the tips relative to the optic axis is given by

$$B_0 = \sqrt{B_x^2 + B_y^2} = \pm G_0 g \ , \tag{4}$$

this implies g in equations 2 and 3 can be written as

$$g = \pm\frac{B_0}{G_0} \ . \tag{5}$$

With $B_z = 0$, the equations of motion for the particles in the x and y axis can be found from the Lorentz equation as,

$$m\frac{d^2x}{dt^2} = (ze)v_z B_y \ , \tag{6}$$

$$m\frac{d^2y}{dt^2} = -(ze)v_z B_x \ , \tag{7}$$

were m is the mass, ze is the charge, and v_z is the component of the velocity of the particles in the z direction. Replacing B_x and B_y from equations 2 and 3, these two equations can be expressed in the following form,

$$\frac{d^2x}{dz^2} = \frac{-(ze)gx}{mv_z} \ , \tag{8}$$

$$\frac{d^2y}{dz^2} = \frac{(ze)gy}{mv_z} \ , \tag{9}$$

where $d^2x/dt^2 = (d^2x/dz^2)(dz/dt)^2$ and $d^2y/dt^2 = (d^2y/dz^2)(dz/dt)^2$. Finally equations 8 and 9 can be expressed in the more compact form of

$$\frac{d^2x}{dz^2} = -k^2x \ , \tag{10}$$

$$\frac{d^2y}{dz^2} = -k^2x \ , \tag{11}$$

where

$$k^2 = \frac{g(ze)}{mv_z} = \pm\frac{B_0(ze)}{G_0 m v_z} \ , \tag{12}$$

and B_0 is in units of Tesla (T), G_0 in meters (m), v_z in ms^{-1} and m is in kg.

The differential equations 10 and 11 describe the particle trajectories in a magnetic quadrupole. On finding solutions (for $k^2 > 0$) and working out the angles of inclination from these equations, the coefficients can be determined if the position and the angle at which the particles entered the quadrupole are known. Thus the

particle trajectories through the quadrupole in the x and y axis are give by the following set of equations,

$$x(z) = x_1 cos(kz) + \frac{tan\alpha_1}{k}\ sin(kz), \tag{13}$$

$$tan\alpha(z) = -x_1 k\ sin(kz)\ + tan\alpha_1\ cos(kz)\ , \tag{14}$$

$$y(z) = y_1 cosh(kz) + \frac{tan\beta_1}{k}\ sinh(kz), \tag{15}$$

$$tan\beta(z) = -y_1 k\ sinh(kz)\ + tan\beta_1\ cosh(kz)\ , \tag{16}$$

where x_1 and y_1 are the positions at which the particles entered the quadrupole in the x-axis and y-axis respectively, while α_1 and β_1 are the angles of inclination at which the particles entered the quadrupole in the x-axis and y-axis respectively.

These solutions are periodic in the xz plane, giving a focusing action toward the optic axis and diverge in the yz plane, therefore defocusing away from the optic axis. The quantity z can be chosen to be the length of the quadrupole w and replacing $tan\alpha$ and $tan\beta$ with a and b respectively, equations 13 to 16 can be rewritten in matrix form as follows,

$$\begin{bmatrix} x_2 \\ a_2 \end{bmatrix} = \begin{bmatrix} A_x & B_x \\ C_x & D_x \end{bmatrix} \begin{bmatrix} x_1 \\ a_1 \end{bmatrix} = \begin{bmatrix} cos(kw) & k^{-1}sin(kw) \\ -ksin(kw) & cos(kw) \end{bmatrix} \begin{bmatrix} x_1 \\ a_1 \end{bmatrix}, \tag{17}$$

$$\begin{bmatrix} y_2 \\ b_2 \end{bmatrix} = \begin{bmatrix} A_y & B_y \\ C_y & D_y \end{bmatrix} \begin{bmatrix} y_1 \\ b_1 \end{bmatrix} = \begin{bmatrix} cosh(kw) & k^{-1}sinh(kw) \\ -ksinh(kw) & cosh(kw) \end{bmatrix} \begin{bmatrix} y_1 \\ b_1 \end{bmatrix}. \tag{18}$$

The refractive power in the lens can be obtained from the C element of the matrices, which for the x-axis gives

$$\frac{1}{f_x} = ksin(kw)\ , \tag{19}$$

and the y-axis as

$$\frac{1}{f_y} = -ksinh(kw)\ . \tag{20}$$

The focusing properties of a quadrupole triplet system are illustrated in Fig.8 which is an illustration of a defocusing-focusing-defocusing (DFD) system. The first quadrupole on the left, defocuses the particles in the x-axis (represented by a concave lens in this axis), the second quadrupole focuses the particles in the x-axis (represented by a convex lens in the x-axis) and the third lens, like the first, is defocusing in the x-axis. The system behaves oppositely in the y-axis, firstly focusing the particles, then defocusing in the second quadrupole and again focusing in the third.

We can describe the particle trajectories through a quadrupole lens system from the first profile plane to the last profile plane by an overall transfer matrix which is a product of several transfer matrices of drift lengths and particle trajectories through the quadrupoles. For a triplet system as in Fig.8 there are seven transfer matrices described by a first drift distance $l1$ (object distance), then the trajectory through the first quadrupole; a second drift distance $d1$, the trajectory through the second quadrupole; a third drift distance $d2$, the trajectory through the third quadrupole; and a fourth drift distance $l2$ (image distance). Also for a triplet system there are two products of seven transfer matrices, one for the x-axis and one for the y-axis, which will differ by a change of sign. The three quadrupoles are characterized by lengths $w1$, $w2$ and $w3$ that each have an associated b-field and aperture size.

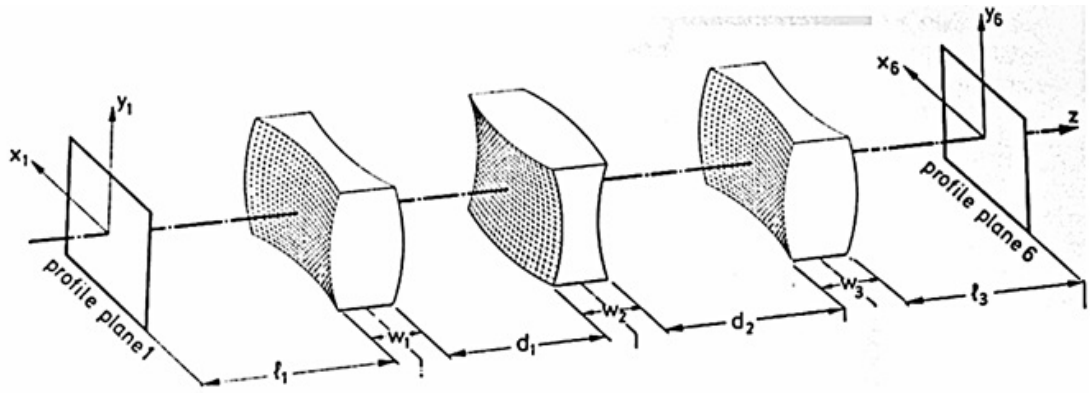

Figure 8: Illustration of a quadrupole triplet DFD system. Where the first quadrupole is defocusing in the x-axis, the second is focusing and the third is again defocusing. The electron beam would propagate from the left-hand side to the right-hand side of the image. Image from Ref. [31].

2.3 Thin-lens Approximation

From equations 17 and 18 it can be seen that the particle trajectories through a quadrupole system made up of a number of lenses and drift distances can be quite complex and difficult, if not impossible to solve analytically. Therefore it must be solved by an iterative numerical procedure. A good starting point to check whether the real system will be technically feasible and also to obtain starting values for a numerical procedure is to treat the quadrupoles as thin lenses and use a thin lens approximation.

As long as kw remains small compared to 1, equations 19 and 20 can be expanded in a power series around $kw = 0$. To zeroth, first and second order these expansions yield

$$f_x = \frac{1}{k^2 w} + \frac{w}{6} + \frac{7k^2 w^3}{360} + \dots \ ,$$

$$f_y = \frac{1}{k^2 w} + \frac{w}{6} + \frac{7k^2 w^3}{360} + \dots \ .$$

By neglecting the higher order terms, these expansions approximate a real quadrupole to a thin lens of focal lengths

$$\frac{1}{f_x} \approx -\frac{1}{f_y} \approx k^2 w \ , \tag{21}$$

which is located at the centre of the quadrupole ($w/2$ from the entrance). For $k_x^2 = -k_y^2 = k^2 > 0$, the necessary k^2 value can be taken from equation 12 to give

$$k_x^2 = -k_y^2 = \pm \frac{B_0(ze)}{G_0 m v_z} \ , \tag{22}$$

where for equations 13 to 16 it is assumed the quadrupole has its focusing in the xz plane and its defocusing in the yz plane. This corresponds to the upper sign in equation 22.

The overall transfer matrix in a thin lens approximation for a triplet system can be described by the following set of seven transfer matrices for both the x and y axis as,

$$\begin{bmatrix} A_x & B_x \\ C_x & D_x \end{bmatrix} = \begin{bmatrix} 1 & \overline{l_2} \\ 0 & 1 \end{bmatrix} \begin{bmatrix} 1 & 0 \\ -\overline{f_3^{-1}} & 1 \end{bmatrix} \begin{bmatrix} 1 & \overline{d^2} \\ 0 & 1 \end{bmatrix} \begin{bmatrix} 1 & 0 \\ -\overline{f_2^{-1}} & 1 \end{bmatrix} \begin{bmatrix} 1 & \overline{d_1} \\ 0 & 1 \end{bmatrix} \begin{bmatrix} 1 & 0 \\ -\overline{f_1^{-1}} & 1 \end{bmatrix} \begin{bmatrix} 1 & \overline{l_1} \\ 0 & 1 \end{bmatrix} , \tag{23}$$

$$\begin{bmatrix} A_y & B_y \\ C_y & D_y \end{bmatrix} = \begin{bmatrix} 1 & \overline{l_2} \\ 0 & 1 \end{bmatrix} \begin{bmatrix} 1 & 0 \\ -\overline{f_3^{-1}} & 1 \end{bmatrix} \begin{bmatrix} 1 & \overline{d^2} \\ 0 & 1 \end{bmatrix} \begin{bmatrix} 1 & 0 \\ -\overline{f_2^{-1}} & 1 \end{bmatrix} \begin{bmatrix} 1 & \overline{d_1} \\ 0 & 1 \end{bmatrix} \begin{bmatrix} 1 & 0 \\ -\overline{f_1^{-1}} & 1 \end{bmatrix} \begin{bmatrix} 1 & \overline{l_1} \\ 0 & 1 \end{bmatrix}, \quad (24)$$

where $\overline{l_1} = l_1 + w_1/2$, $\overline{d_1} = d_1 + (w_1 + w_2)/2$, $\overline{d_2} = d_2 + (w_2 + w_3)/2$, $\overline{l_2} = l_2 + w_3/2$, $-\overline{f_1^{-1}} \approx k_1^2 w_1$, $-\overline{f_2^{-1}} \approx k_2^2 w_2$, $-\overline{f_3^{-1}} \approx k_3^2 w_3$.

If the lengths, aperture size and the magnetic field strength of the quadrupoles are known, along with the particle charge, mass and velocity then equation 22 can be used to find the approximate thin lens focal lengths of the quadrupoles, hence the particle trajectories through them can be determined.

The aim of this study is to determine the magnetic field strength B (in Tesla) and length w of three quadrupoles, along with the separation between them d_1 and d_2, the object distance l_1 (the distance between the electron beam and the first quadrupole) and the image distance l_2 (the distance between the exit of the last quadrupole and the lead target). These quadrupoles will be used to focus an electron beam with maximum energy (E) of 600 MeV and a full-width half-maximum divergence of 5 mrad, that must be converged onto a lead target at an angle of -20 mrad so as to trigger the electromagnetic cascade which will result in generating a collimated neutral electron-positron beam. At this energy the electrons are moving at relativistic speeds, therefore the increased mass m and the relativistic velocity v can be found from the relations,

$$m = m_0(1 + 2\eta) \ , \quad (25)$$

$$v = 13.891 \frac{\sqrt{E(1+\eta)/m_0}}{1 + 2\eta} \ , \quad (26)$$

where m_0 is the rest mass and $\eta = E/2m_0c^2$. Here m and m_0 are in atomic mass units (u), E is in MeV and v is in $m\ \mu s^{-1}$. These values can then be converted into SI units and used to calculate each value of k^2. If a DFD system is used, then the first quadrupole has its defocusing (D) action in the xz plane and its focusing (F) action in the yz plane. The appropriate sign for the k^2 values in both the x and y axis can then be obtained from equation 22. [34]

To obtain the required parameters the problem is set-up in the mathematical computation program MATLAB (see Appendix A for code). The values G_0, B_1, B_2, B_3, w_1, w_2, w_3, d_1 and d_2 are all set as variables within the problem, although these themselves are constrained to within limits. Since the experiment will be contained within a vacuum chamber of limited room, the overall length of the collimating system (from the start of the electron beam to the lead target) must be kept to approximately one metre. Due to the availability and size of miniature quadrupoles, the magnetic field strength must not exceed 1.2 T [33] and the aperture $2G_0$ needs to be ~ 6 mm. With the length of the quadrupoles kept approximately between 15-60 mm, if the quadrupoles get much longer than this then the thin lens approximation starts to break down. If equation 22 is to hold then the aperture size needs to stay smaller than approximately $w/2$, this is to ensure that large fringing field action does not occur. Also due to fringing fields it is desirable to have a separation between the quadrupoles greater than 40 mm.

Using various values for the variables the system matrix of the system (the overall transfer matrix minus the first and last drift lengths) can be calculated. Representing the elements of the system matrix as A_s, B_s, C_s and D_s, the overall transfer matrix can be written as

$$\begin{bmatrix} A & B \\ C & D \end{bmatrix} = \begin{bmatrix} 1 & \overline{l_2} \\ 0 & 1 \end{bmatrix} \begin{bmatrix} A_s & B_s \\ C_s & D_s \end{bmatrix} \begin{bmatrix} 1 & \overline{l_1} \\ 0 & 1 \end{bmatrix} = \begin{bmatrix} A_s + C_s\overline{l_2} & A_s\overline{l_1} + C_s\overline{l_2 l_1} + B_s + D_s\overline{l_2} \\ C_s & C_s\overline{l_1} + D_s \end{bmatrix}. \quad (27)$$

Adding in the position vectors to determine the electron transfer from the first profile plane to the last profile plane and knowing that for a point-to-point focusing system requires the B element in the overall transfer matrix to be set to zero, $\overline{l_1}$ and $\overline{l_2}$ can be found as follows.

$$\begin{bmatrix} x_2 \\ a_2 \end{bmatrix} = \begin{bmatrix} A & 0 \\ C & D \end{bmatrix} \begin{bmatrix} 0 \\ a_1 \end{bmatrix} \quad (28)$$

Equation 28 (showing here for the xz plane only, but the same can be said of the yz plane) implies that $x_2 = 0$, since $x_1 = 0$ as we are considering the electron beam coming from a point source and focusing on the optical z-axis. The value of the D element can now be found from the equation, since $a_2 = a_1 D$, where the initial angle of the electron beam from the z-axis is $a_1 = 2.5$ mrad and the converging angle of

the electron beam going into the lead target is $a_2 = 10$ mrad from the z-axis. This gives a value $D = -4$, that can now be set equal to the D element in equation 27 and rearranged to find $\overline{l_1}$ given by,

$$\overline{l_1} = \frac{-4 - D_s}{C_s} \ . \tag{29}$$

$\overline{l_2}$ can now be found by setting the B element in equation 27 to zero and rearranging to give,

$$\overline{l_2} = \frac{-A_s\overline{l_1} - B_s}{C_s\overline{l_1} + D_s} \ . \tag{30}$$

The overall length of the system (*overall*) can then be calculated by adding together $\overline{l_1}$, $\overline{d_1}$, $\overline{d_2}$, $\overline{d_3}$ and $\overline{l_2}$. The maximum spread (max_x) of the electron beam in any DFD triplet system occurs in the x-axis of the middle quadrupole and can be found from geometry as,

$$max = 2tan\alpha_1(\overline{l_1} + \overline{d_1} - (\overline{d_1 l_1}/\overline{f_1})) \ , \tag{31}$$

this is an important parameter and needs to be kept smaller than the diameter of the aperture.

Table 1: A selection of results obtained for $\overline{l_{1x}}$ and $\overline{l_{1y}}$ plotted as a function of d_1, for a constant d_2 = 5.0 cm, each time varying the size of the aperture radius G_0. These were found with quadrupoles set for w_1 = 2.0 cm, w_2 = 5.0 cm, w_3 = 5.0 cm, B_1 = 1.1 T, B_2 = 1.2 T and B_3 = 1.2 T. The first set of data for G_0=0.003 m is the optimal values for the triplet set-up.

$G_0 = 0.003$ m				
$d_1 = 11.50$ cm	$\overline{l_{1x}} = 55.40$ cm	$\overline{l_{2x}} = 7.609$ cm	$overall_x = 88.011$ cm	$max_x = 5.041$ mm
$d_1 = 11.50$ cm	$\overline{l_{1y}} = 55.69$ cm	$\overline{l_{2y}} = 17.44$ cm	$overall_y = 98.13$ cm	$max_y = 2.005$ mm
$G_0 = 0.0025$ m				
$d_1 = 8.800$ cm	$\overline{l_{1x}} = 35.58$ cm	$\overline{l_{2x}} = 3.083$ cm	$overall_x = 60.96$ cm	$max_x = 3.355$ mm
$d_1 = 8.800$ cm	$\overline{l_{1y}} = 35.55$ cm	$\overline{l_{2y}} = 14.33$ cm	$overall_y = 72.18$ cm	$max_y = 1.432$ mm
$G_0 = 0.002$ m				
d1 = 8.300 cm	$\overline{l_{1x}} = 16.56$ cm	$\overline{l_{2x}} = -0.9074$ mm	$overall_x = 38.27$ cm	$max_x = 1.955$ mm
$d_1 = 8.300$ cm	$\overline{l_{1y}} = 16.57$ cm	$\overline{l_{2y}} = 11.24$ cm	$overall_y = 49.60$ cm	$max_y = 0.8816$ mm

As a starting point a range of values for the maximal spread in the electron beam max_x were plotted as a function of the aperture radius G_0, for a range of B-fields,

magnet lengths and drift lengths (d_1 and d_2). A typical trend for this data in Fig.9 shows that as the aperture size is increased the max_x value rapidly increases. Similar such trends were also obtained for the overall length of the system as a function of G_0. In both cases it is better to have a smaller overall length and max_x spread, implying that a smaller aperture is preferable, but there is a pay-off for this with the size of the drift lengths. As an example, a selection of data in Table 1 shows that as G_0 is decreased $\overline{l_x}$ becomes very small (imaginary image for $G_0 = 0.002$ m). Considering that this value would have to be reduced by 2.5 cm for l_x, this would make it an unrealistic length in which to insert a target. Therefore an aperture radius of $G_0 = 0.003$ m for all three quadrupoles was settled on.

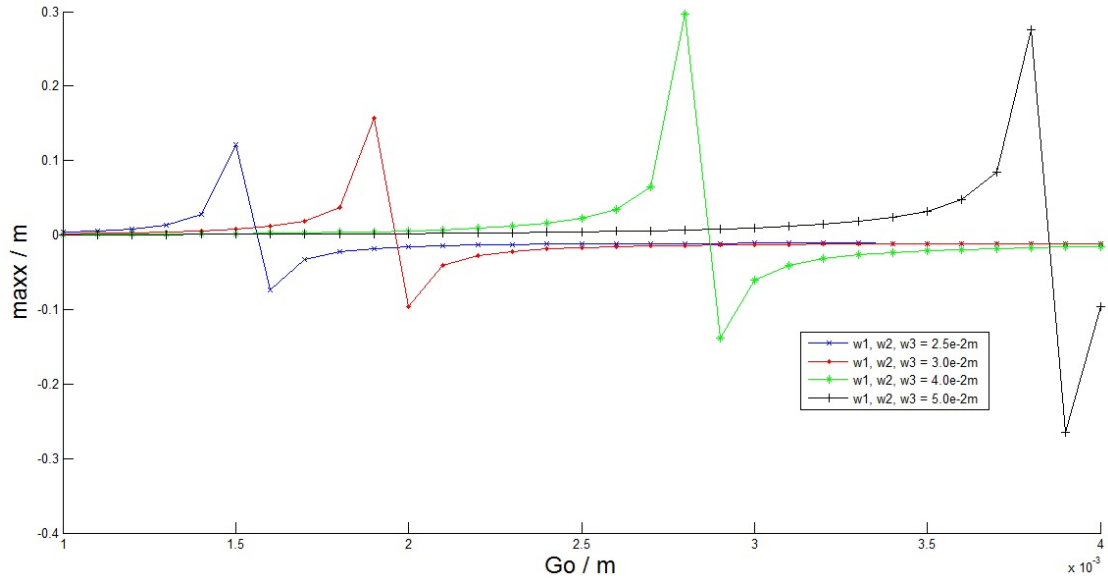

Figure 9: max_x as a function of the aperture radius G_0 for a range of values w_1, w_2 and w_3, shows how max_x rapidly increases for an increasing aperture size. Found with quadrupoles set for $d_1 = 11.50$ cm, $d_2 = 5.0$ cm, $G_0 = 0.003$ m, $B_1 = 1.2$ T, $B_2 = 1.2$ T and $B_3 = 1.2$ T. With lines between the data points for a guide to the eye.

Due to the change of sign in the x and y planes, two different sets of values are obtained from the thin lens approximations. It is a necessary requirement to keep the object length for both these planes the same and as shown in Fig.10 this value can be found by plotting $\overline{l_{1x}}$ and $\overline{l_{1y}}$ together as a function of drift distance d_1 ,while d_2 is held constant and find the point at which the plots cross, which can be seen more clearly when zoomed in Fig.11. This is repeated for a number of arrangements

and values for the quadrupoles, where each time the results for the overall length, maximum electron spread and image length $\overline{l_2}$ are checked to see if they lie within the parameters required.

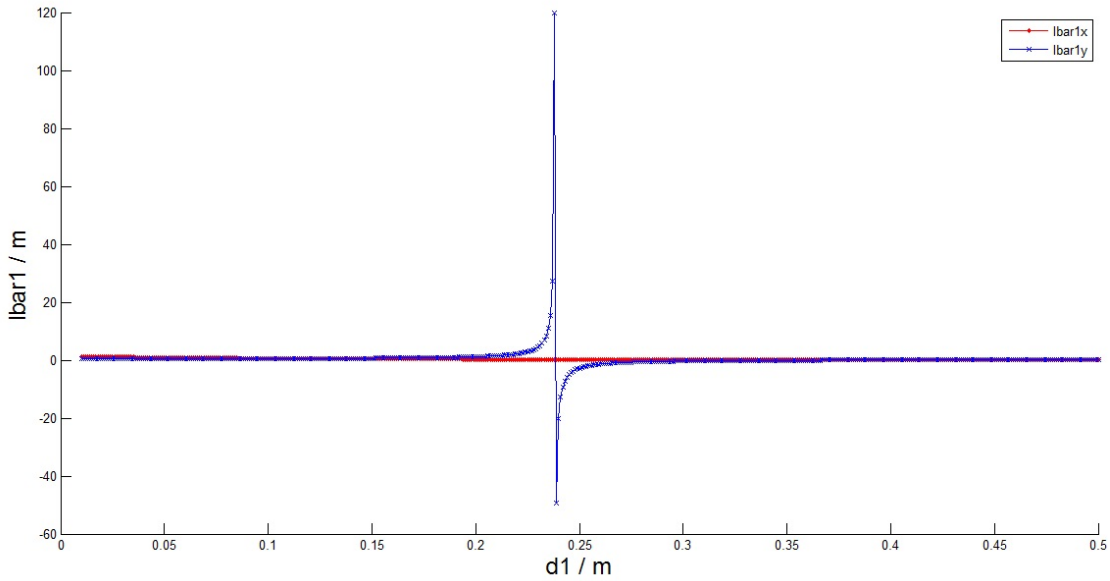

Figure 10: $\overline{l_{1x}}$ and $\overline{l_{1y}}$ as a function of d_1. Found with quadrupoles set for $d_2 = 5.0$ cm, $G_0 = 0.003$ m, $w_1 = 2.0$ cm, $w_2 = 5.0$ cm, $w_3 = 5.0$ cm, $B_1 = 1.1$ T, $B_2 = 1.2$ T and $B_3 = 1.2$ T. This plot gives the overall optimal values for the system at the point were $\overline{l_{1x}}$ and $\overline{l_{1y}}$ cross. With lines between the data points for a guide to the eye.

Narrowing down the focusing strength of each quadrupole (i.e. the longer the quadrupole and the higher the B-field, the stronger the focusing) becomes apparent when plots are produced. If the focusing strength is too weak, $\overline{l_{1x}}$ and $\overline{l_{1y}}$ do not converge within the required overall length of the system and if it is too strong then $\overline{l_{2x}}$ becomes too small. If the centre quadrupole has a smaller focusing strength than the two end lenses then minus numbers are given out for $\overline{l_{1x}}$ and $\overline{l_{1y}}$ (see Fig.12). Therefore the best set-up is found when the second and third lenses are strong focusing and the first quadrupole is weaker. This can also be fine tuned by increasing or decreasing the length of d_2. By increasing the length, the maximum beam spread and overall length become smaller, but again $\overline{l_{2x}}$ becomes too small.

Finally the optimal parameters are found to be, for the x plane, $\overline{l_{1x}} = 55.40$ cm, $d_1 = 11.50$ cm, $d_2 = 5.0$ cm, $\overline{l_{2x}} = 7.609$ cm, $overall_x = 88.01$ cm and $max_x = 5.041$

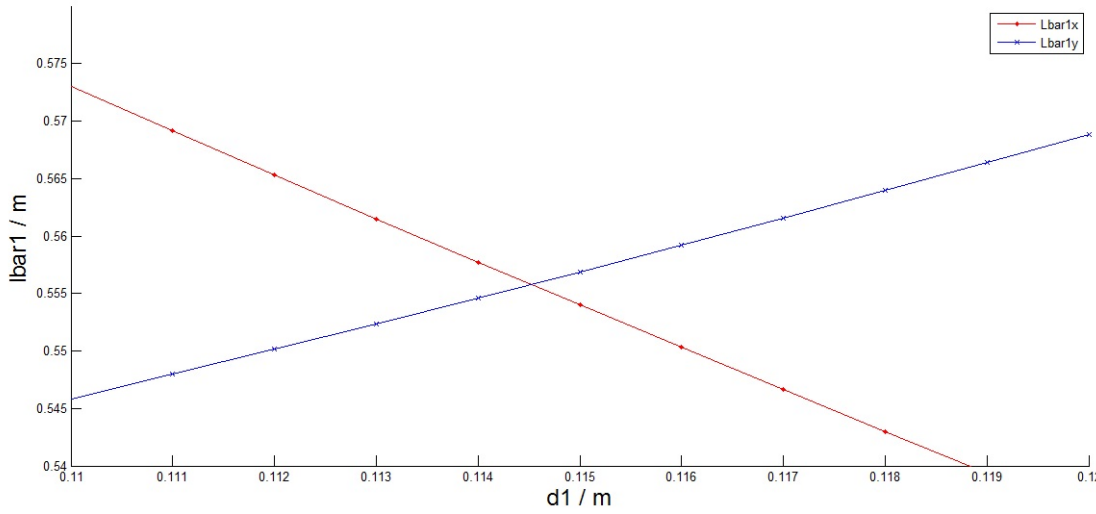

Figure 11: Zoomed in view of Fig.10 for the converging point $\overline{l_{1x}}$ and $\overline{l_{1y}}$ as a function of d_1. Found with quadrupoles set for $d_2 = 5.0$ cm, $G_0 = 0.003$ m, $w_1 = 2.0$ cm, $w_2 = 5.0$ cm, $w_3 = 5.0$ cm, $B_1 = 1.1$ T, $B_2 = 1.2$ T and $B_3 = 1.2$ T. This plot gives the overall optimal values for the system at the point were $\overline{l_{1x}}$ and $\overline{l_{1y}}$ cross. With lines between the data points for a guide to the eye.

mm. For the y plane these are $\overline{l_{1y}} = 55.69$ cm, $d_1 = 11.50$ cm, $d_2 = 5.0$ cm, $\overline{l_{2y}} = 17.44$ cm, $overall_y = 98.13$ cm and $max_y = 2.005$ mm. These parameters were found with quadrupoles set for $G_0 = 0.003$ m, $w_1 = 2.0$ cm, $w_2 = 5.0$ cm, $w_3 = 5.0$ cm, $B_1 = 1.1$ T, $B_2 = 1.2$ T and $B_3 = 1.2$ T.

3 Simion Simulations

3.1 Simion Introduction

To solve the trajectories of the electron beam through the quadrupoles numerically and to give a good visual look at what is happening with the electron beam between the quadrupoles and at the focus point, a simulation software package called Simion is used, which is an "ion optics simulation program that calculates magnetic and electric fields for electrodes of defined voltages and the ion trajectories in those fields" [35].

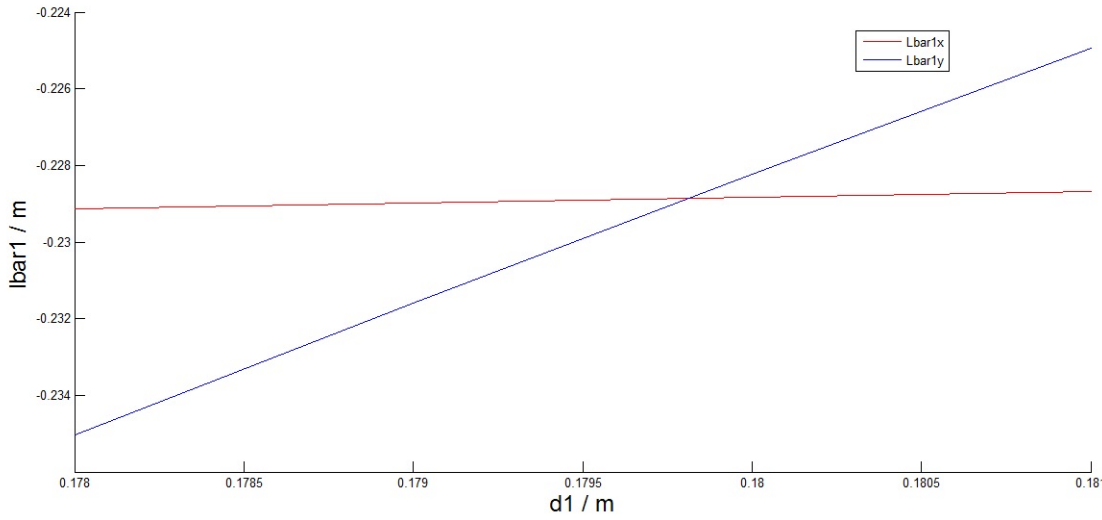

Figure 12: The converging point for $\overline{l_{1x}}$ and $\overline{l_{1y}}$ as a function of d_1, giving a minus valued object length. Were the centre quadrupole has a stronger focusing strength than the two end lenses. Found with quadrupoles set for $d_2 = 5.0$ cm, $G_0 = 0.003$ m, $w_1 = 5.0$ cm, $w_2 = 2.0$ cm, $w_3 = 5.0$ cm, $B_1 = 1.2$ T, $B_2 = 1.1$ T and $B_3 = 1.2$ T. With lines between the data points for a guide to the eye.

3.2 Electron Beam Energy of 600 MeV

On using the optimal parameters in section 2.3 to build up the quadrupoles along with setting the drift lengths between them within this program, the electron beam is then flown through at the previously defined values. This simulation can be seen in Fig.13 for the x,z plane which shows the electrons propagating from the right hand side to the left hand side. It can be seen that the electrons do indeed focus to a point, which is also true for the y,z plane. Fig.14 gives a zoomed in view of the system along with some cut throughs in the x,y plane to show how the electrons are focused and defocused as they travel through the quadrupoles. Notice in the middle quadrupole that we have the maximum spread of the electrons in the x-axis. This simulation gave a converging angle of -15.6 mrad in the x,z plane and a converging angle of -16.0 mrad in the y,z plane.

The parameters of the system are then adjusted within Simion (see section 3.1) to see if better results can be obtained. It is found by decreasing the magnetic field strength of B_1 the elevation of the electron beam quickly rises, while the azimuth fluctuates slightly. By increasing the length of l_1 the azimuth increases quickly, while

the elevation increases slightly. If these are both increased together then an elevation and azimuth angle close to that of which is required can be obtained.

Therefore by resetting the first quadrupole to $B_1 = 0.9$ T, and increasing the object length to $l_1 = 60.4$ cm, this gave a converging angle of -19.8 mrad in the x,z plane and a converging angle of -20.3 mrad in the y,z plane. Along with new values for $overall = 94.7$ cm, $max_x = 5.1$ mm $\pm$ 0.1 mm and a minimum $l_2 = 5.0$ cm.

These converging angles are to within a few tenths of mrad of what is required for an electron beam to initiate a quantum electrodynamic cascade in order to produce a collimated electron-positron beam, making these parameters for the quadrupoles good enough to take into the laboratory to experimentally optimise the electron beam focusing system. The thin lens approximation turned out to be a good analytical method to obtain starting values for a numerical procedure, since not much adjusting had to be done within the numerical model to produce accurate results. The most important parameters such as the overall length of the system ($overall$) and the maximum spread in the electron beam (max_x), being comparable to within a few tenths of the values obtained for the thin lens approximations.

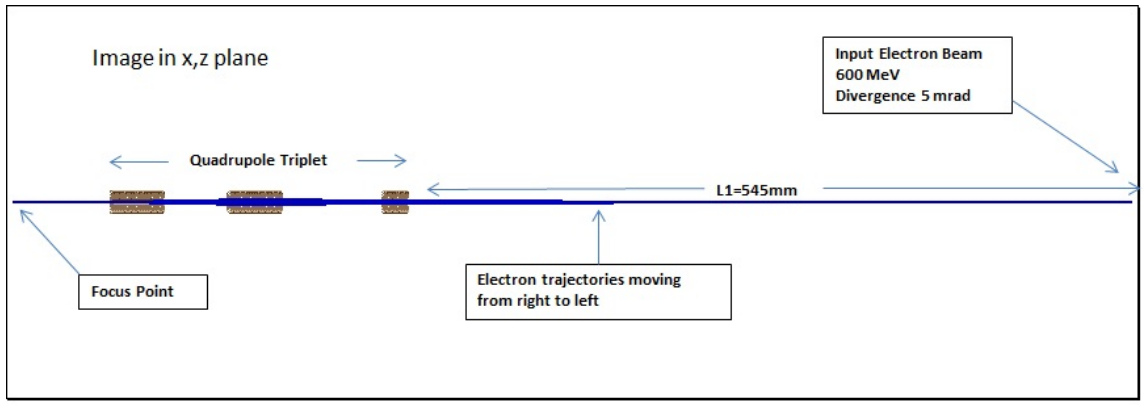

Figure 13: Simion simulation showing the flight of electrons propagating from the right hand side to the left hand side in the x,z plane, through a magnetic quadrupole triplet system set to the thin lens approximation optimal values. With electron beam energy of $E = 600$ MeV.

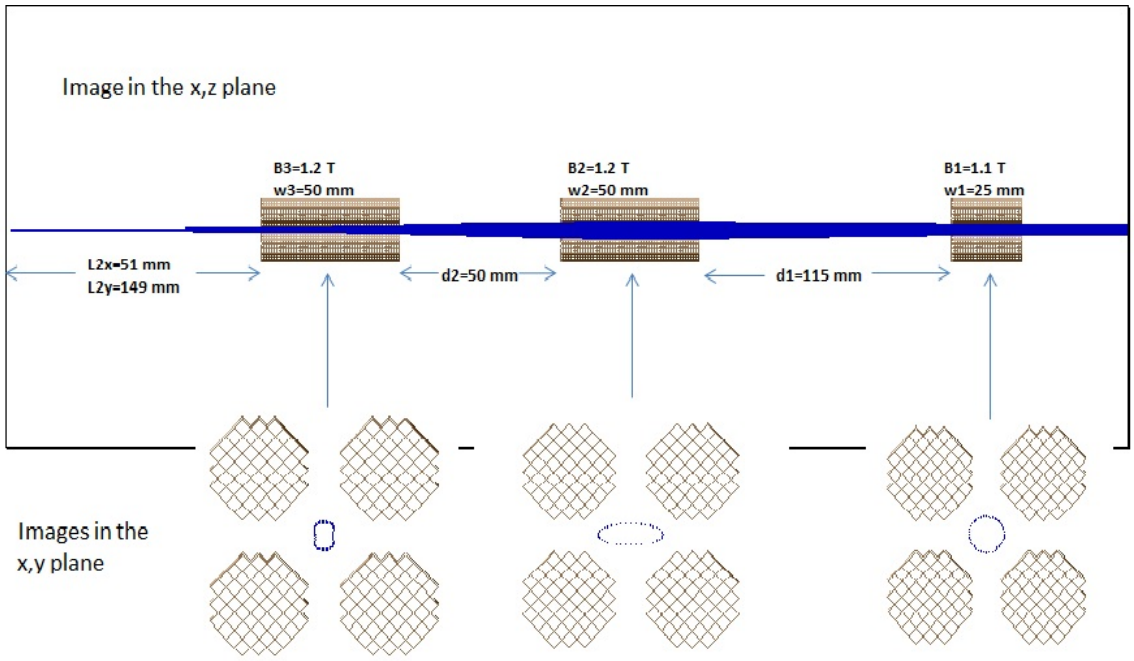

Figure 14: Zoomed in view of the triplet system of Fig.13, with the flight of electrons propagating from the right hand side to the left hand side in the x,z plane. It can be clearly seen that the electron beam does converge to the focus point on exiting the last quadrupole. Also shown are three cut throughs of the quadrupoles in the x,y plane to show how the electrons are focused and defocused through the quadrupoles. Notice in the middle quadrupole that there is a the maximum spread of the electrons in the x-axis.

3.3 Electron Beam Energy of 600 MeV and 30 mrad Converging Angle

The 20 mrad diverging angle of the electron-positron beam after leaving the lead target is an approximation, and it would be useful if the angle of the converging electron beam incident onto this lead target could be controlled to give a range of values that may be required to collimate the neutral pair beam.

Here we look at the case of collimating a diverging 30 mrad electron-positron beam with a converging electron beam of 30 mrad incident onto the lead target. Firstly the value of the D element in equation 27 is re-evaluated for the converging angle of the electron beam going into the lead target from the z-axis. This now

becomes $a_2 = 15$ mrad, giving a value $D = -6$.

Keeping the values of the quadrupole lenses the same as in section 3.2 and only changing the drift distances, this gives optimal thin lens approximations for the x,z plane as, $\overline{l_{1x}} = 73.3$ cm, $d_1 = 8.60$ cm, $d_2 = 5.0$ cm, $\overline{l_{2x}} = 3.47$ cm, $overall_x = 1.01$ m and $max_x = 5.89$ mm. For the y,z plane these are $\overline{l_{1y}} = 7.33$ cm, $d_1 = 86.0$ cm, $d_2 = 5.0$ cm, $\overline{l_{2y}} = 16.0$ cm, $overall_y = 1.13$ m and $max_y = 2.65$ mm. These parameters were found with quadrupoles set for $G_0 = 0.003$ m, $w_1 = 2.0$ cm, $w_2 = 5.0$ cm, $w_3 = 5.0$ cm, $B_1 = 1.1$ T, $B_2 = 1.2$ T and $B_3 = 1.2$ T.

These values for the thin lens approximation when entered directly into Simion (see section 3.1) gave a converging angle of -19.8 mrad in the x,z plane and a converging angle of -22.1 mrad in the y,z plane. After adjusting in Simion, bringing the magnetic field strength of the first quadrupole down to $B_2 = 0.9$ T, decreasing the length of d_1, increasing the length of d_2, and increasing the length of l_1, this gave a converging angle of -30.0 mrad in the x,z plane and a converging angle of -30.1 mrad in the y,z plane. Along with new values for $overall = 1.02$ m, $max_x = 5.6$ mm $\pm$ 0.2 mm and a minimum $l_2 = 6.0$ mm.

On entering the thin lens approximations directly into Simion, this gave a converging electron beam in both axis into the image plane, although the converging angles were on the order of 10 mrad off from that which is required (-30 mrad). These values still proved to be a good starting point for the numerical simulation and after some adjustments within Simion, converging angles to within a tenth of a mrad to that which is required were obtained, along with the most important parameters such as the overall length of the system ($overall$) and the maximum spread in the electron beam (max_x), being comparable to within a few tenths of the values obtained for the thin lens approximations.

Although the length of l_2 is very small, it is still possible to insert a target at this point and since the lens values have been kept the same as in section 3.2 this shows that the focusing system can be adjusted for a range of converging angles onto the target.

3.4 Electron Beam Energy of 200 MeV

To see if the same quadrupoles could be used for a lower electron energy of 200 MeV to achieve the same converging angle, thin lens approximations were carried

out using the same lens values as before for the 600 MeV case. At this new energy the best arrangement for the quadrupoles to achieve the optimal focus is to have the lens with the lowest magnetic field strength in the central position, along with changing the lengths of the drift distances. The new parameters are found to be, for the x,z plane, $\overline{l_{1x}}$ = 3.033 cm, d_1 = 48.3 m, d_2 = 5.6 cm, $\overline{l_{2x}}$ = 4.395 cm, $overall_x$ = 68.33 m and max_x = 5.091 mm. For the y,z plane these are $\overline{l_{1y}}$ = 3.0316 cm, d_1 = 48.3 cm, d_2 = 5.6 cm, $\overline{l_{2y}}$ = 4.144 cm, $overall_y$ = 68.075 cm and max_y = 0.3936 mm. These parameters were found with quadrupoles set for G_0 = 0.003 m, w_1 = 5.0 cm, w_2 = 2.0 cm, w_3 = 5.0 cm, B_1 = 1.2 T, B_2 = 1.1 T and B_3 = 1.2 T.

These values for the thin lens approximation when entered directly into Simion (see section 3.1) made the electron beam converge too quickly and come to focus in the third lens in the x-axis before starting to diverge on exit of the lens. After adjusting in Simion, increasing the second drift distance to d_2 = 6.3 cm by moving the third lens, bringing the magnetic field strength of the second quadrupole down to B_2 = 0.9 T and slightly increasing the object distance to l_1 = 8.4 mm, this gave a converging angle of -19.6 mrad in the x,z plane and a converging angle of -20.1 mrad in the y,z plane. Along with new values for $overall$ = 69.4 cm, max_x = 5.7 mm ± 0.2 mm and a minimum l_2 = 2.0 cm.

To see if accurate converging angles could be achieved by adjusting the set-up differently the second lens was moved towards the first lens decreasing the first drift distance to d_1 = 47.5 cm and increasing the second drift distance to d_2 = 6.4 cm, bringing the magnetic field strength of the second quadrupole down to B_2 = 0.9 T and slightly increasing the object distance to l_1 = 8.5 mm, this gave a converging angle of -20.0 mrad in the x,z plane and a converging angle of -19.7 mrad in the y,z plane. Along with new values for $overall$ = 68.6 cm, max_x = 5.6 mm ± 0.2 mm and a minimum l_2 = 1.8 cm.

Even though the thin lens approximations, when put directly into Simion converged the electron beam too quickly in the third lens and therefore not converging to a point in the image plane, these values still proved to be a good starting point for the numerical simulation. After some fine adjustments within Simion for both set-ups, converging angles to within a few tenths of mrad of what is required (-20 mrad) were obtained, along with the most important parameters such as the overall length of the system ($overall$) and the maximum spread in the electron beam (max_x), being comparable to within a few tenths of the values obtained for the thin

lens approximations.

Having used the same strength quadrupoles as for the 600 MeV electron beam energy, it has been shown that the quadrupole triplet set-up is a dynamic system that can be used for a range of energies. Also it has been demonstrated that there is more than one way to fine adjust the quadrupoles to achieve this goal, which will prove useful in a laboratory experimental set-up.

3.5 Electron Beam Energy of 200 MeV and Changing One Quadrupole

Since the object and image distance in the previous set-up is quite tight, one quadrupole was changed out to see if these values could be increased. The new parameters for the optimal thin lens approximation are found to be, for the x,z plane, $\overline{l_{1x}} = 5.810$ cm, $d_1 = 48.8$ cm, $d_2 = 5.5$ cm, $\overline{l_{2x}} = 4.749$ cm, $overall_x = 70.86$ cm and $max_x = 5.306$ mm. For the y,z plane these are $\overline{l_{1y}} = 5.808$ cm, $d_1 = 48.8$ cm, $d_2 = 5.5$ cm, $\overline{l_{2y}} = 4.124$ cm, $overall_y = 70.23$ cm and $max_y = 0.405$ mm. These parameters were found with quadrupoles set for $G_0 = 0.003$ m, $w_1 = 3.0$ cm, $w_2 = 2.0$ cm, $w_3 = 5.0$ cm, $B_1 = 1.1$ T, $B_2 = 1.1$ T and $B_3 = 1.2$ T.

These values for the thin lens approximation when entered directly into Simion (see section 3.1) made the electron beam converge too quickly and come to focus in the third lens in the x-axis before starting to diverge on exit of the lens. After adjusting in Simion, increasing the second drift distance to $d_2 = 6.5$ cm by moving the third lens, bringing the magnetic field strength of the second quadrupole down to $B_2 = 0.9$ T and slightly decreasing the object distance to $l_1 = 4.16$ cm, this gave a converging angle of -20.0 mrad in the x,z plane and a converging angle of -20.0 mrad in the y,z plane. Along with new values for $overall = 71.0$ cm, $max_x = 5.5$ mm $\pm$ 0.2 mm and a minimum $l_2 = 1.5$ cm.

To see if accurate converging angles could be achieved by adjusting the set-up differently the second lens was moved towards the first lens decreasing the first drift distance to $d_1 = 47.6$ cm and increasing the second drift distance to $d_2 = 6.7$ cm, bringing the magnetic field strength of the second quadrupole down to $B_2 = 0.9$ T and slightly decreasing the object distance to $l_1 = 4.18$ cm, this gave a converging angle of -20.4 mrad in the x,z plane and a converging angle of -20.4 mrad in the y,z plane. Along with new values for $overall = 69.6$ cm, $max_x = 5.3$ mm $\pm$ 0.2 mm

and a minimum $l_2 = 1.1$ cm.

Even though the thin lens approximations, when put directly into Simion converged the electron beam too quickly in the third lens and therefore not converging to a point in the image plane, these values still proved to be a good starting point for the numerical simulation. After some fine adjustments within Simion for both set-ups, converging angles to within a few tenths of mrad of what is required (-20 mrad) were obtained (accurate to within three significant figures for the first set-up), along with the most important parameters such as the overall length of the system (*overall*) and the maximum spread in the electron beam (max_x), being comparable to within a few tenths of the values obtained for the thin lens approximations.

This gives similar results to section 3.4 with the advantage of the object length increasing.

3.6 Electron Beam Energy of 200 MeV and Changing Two Quadrupoles

Again similar to the last section but this time two quadrupoles are changed out from section 3.4, to see how this changes the system and if a longer image distance can be achieved. The new parameters for the optimal thin lens approximation are found to be, for the x,z plane, $\overline{l_{1x}} = 5.195$ cm, $d_1 = 47.7$ cm, $d_2 = 5.5$ cm, $\overline{l_{2x}} = 5.611$ cm, $overall_x = 69.51$ cm and $max_x = 4.91$ mm. For the y,z plane these are $\overline{l_{1y}} = 5.216$ cm, $d_1 = 47.7$ cm, $d_2 = 5.5$ cm, $\overline{l_{2y}} = 6.265$ cm, $overall_y = 70.18$ cm and $max_y = 0.617$ mm. These parameters were found with quadrupoles set for $G_0 = 0.003$ m, $w_1 = 3.0$ cm, $w_2 = 2.0$ cm, $w_3 = 4.0$ cm, $B_1 = 1.1$ T, $B_2 = 1.1$ T and $B_3 = 1.1$ T.

These values for the thin lens approximation when entered directly into Simion (see section 3.1) made the electron beam converge too quickly and come to focus in the third lens in the x-axis before starting to diverge on exit of the lens. After adjusting in Simion, increasing the second drift distance to $d_2 = 6.5$ cm by moving the third lens, bringing the magnetic field strength of the second quadrupole down to $B_2 = 0.9$ T and slightly decreasing the object distance to $l_1 = 3.70$ cm, this gave a converging angle of -19.2 mrad in the x,z plane and a converging angle of -19.4 mrad in the y,z plane. Along with new values for $overall = 70.2$ cm, $max_x = 5.0$ mm $\pm$ 0.2 mm and a minimum $l_2 = 3.3$ cm.

To see if accurate converging angles could be achieved by adjusting the set-up

differently the second lens was moved towards the first lens decreasing the first drift distance to $d_1 = 46.4$ cm and increasing the second drift distance to $d_2 = 6.8$ cm, bringing the magnetic field strength of the second quadrupole down to $B_2 = 0.9$ T and slightly increasing the object distance to $l_1 = 3.76$ cm, this gave a converging angle of -20.1 mrad in the x,z plane and a converging angle of -20.1 mrad in the y,z plane. Along with new values for $overall = 68.4$ cm, $max_x = 4.9$ mm $\pm$ 0.2 mm and a minimum $l_2 = 2.4$ cm.

Even though the thin lens approximations, when put directly into Simion converged the electron beam too quickly in the third lens and therefore not converging to a point in the image plane, these values still proved to be a good starting point for the numerical simulation. After some fine adjustments within Simion for both set-ups, converging angles to within a few tenths of mrad of what is required (-20 mrad) were obtained, along with the most important parameters such as the overall length of the system ($overall$) and the maximum spread in the electron beam (max_x), being comparable to within a few tenths of the values obtained for the thin lens approximations.

Again this gives similar results to section 3.4 with the advantage of not only the object length increasing, but also the image length increasing.

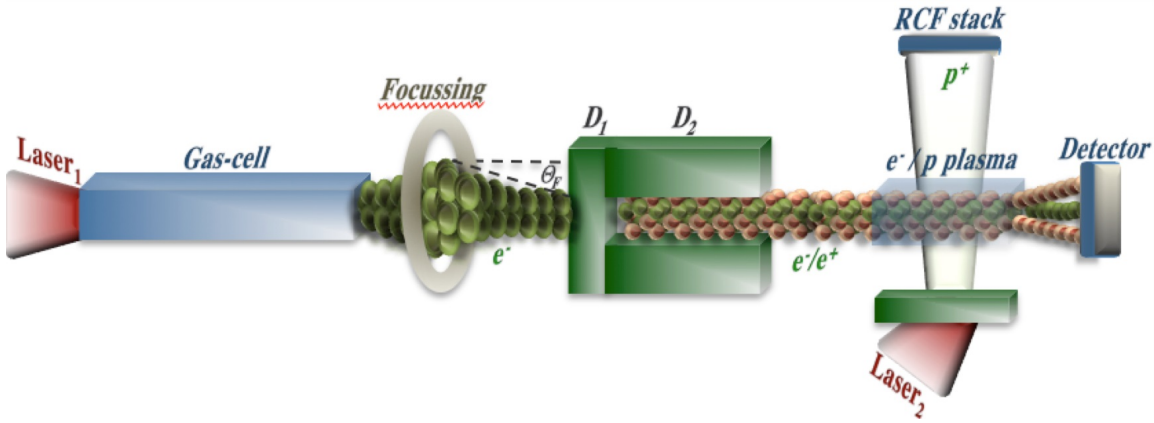

Figure 15: An illustration of a proposed experimental set-up, consisting of an electron beam focussing system incident on a high density target. The envisaged collimated electron-positron beam will then be directed onto a low density gas and transversally probed using a proton imaging technique, to study any instabilities that may cause filamentation of the beam to occur. Image from Ref. [31].

4 Conclusion

The aim of this project is to use a system comprising of three miniature quadrupoles to focus a diverging electron beam with an initial spread of 5 mrad onto a lead solid target with a converging angle of -20 mrad, this will initiate an electrodynamic cascade within the solid to produce a collimated neutral electron-positron beam.

These results show numerically and analytically that it is possible to get very close to the converging angle of -20 mrad that is needed in order to initiate a quantum electrodynamic cascade, whilst keeping the length of the system and the overall parameters of the quadrupoles to within the required values. This shows that for the range of values used within this study, a thin lens approximation is a viable and accurate analytical method to use in order to gain a good starting point to check whether the real system will be technically feasible and also to obtain starting values for a numerical procedure. It has also been demonstrated that this system of lenses is a highly dynamical system that can be used for a range of energy values and converging angles by simply rearranging the lenses or adjusting the drift distances between them. By changing out only one lens in the set-up, this system can take on a further range of values allowing it to be tailored to specific requirements. This is seen to be of great benefit due to the high expense in producing miniature magnetic quadrupoles.

The next step is to take this into the laboratory to experimentally optimise this electron beam focussing system and then use this focussed beam to trigger the electromagnetic cascade to generate the neutral electron-positron beam. As seen in Fig.15 of a proposed experiment, this can then be directed into a low density gas in order to study any instabilities that develop which will cause the electron-positron beam to filament, leading to the generation of strong magnetic fields.

On completion the focusing of this beam is seen to represent a ground breaking experiment in its own right, as it would open up a new field of research for study of neutral pair plasmas as well as reproducing for the first time some of the astronomical phenomenon as previously discussed.

References

[1] R. D. Blandford and R. L. Znajek. Electromagnetic extraction of energy from Kerr black holes. *Mon. Not. R. Astron. Soc.*, 179:433–456, 1977.

[2] M. C. Begelman, R. D. Blandford, and M. J. Rees. Theory of extragalactic radio sources. *Rev. Mod. Phys.*, 56:255–351, 1984.

[3] J. F. C. Wardle, D. C. Homan, R. Ojha, and D. H. Roberts. Electron-positron jets associated with the quasar 3C279. *Nature*, 395:457–461, 1998.

[4] W. Kundt and Gopal-Krishna. Extremely relativistic electron-positron twin-jets form extragalactic radio sources. *Nature*, 288:149–150, 1980.

[5] A. V. Gurevich and I. N. Istomin. Production of an electron-positron plasma in a pulsar magnetosphere. *Zh. Eksp. Teor. Fiz.*, 89:3–21, 1985.

[6] I. A. Rylov. Electron-positron pairs production in the pulsar magnetosphere. *Astrophy. Space Sci.*, 75:423–436, 1981.

[7] R. Moll. *Magnetic Acceleration and Instabilities of Astrophysical Jets.* Universiteit van Amsterdam [Host]. Available at http://www.astro.uva.nl/static/research/theses/phd/r-moll.pdf, 2010.

[8] M. Georganopoulos, D. Kazanas, E. E. Perlman, and F. W. Stecker. Bulk comptonization of the cosmic microwave background by extragalactic jets as a probe of their matter content. *Astrophys. J.*, 625:656–666, 2005.

[9] P. Chang, A. Spitkovsky, and J.A. Arons. Long-term evolution of magnetic turbulence in relativistic collisionless shocks: electron-positron plasmas. *Astrophys. J.*, 674(1):378, 2008.

[10] J. M. Laming. Collisionless shock wave. *Scholarpedia*, 4(7):6071, 2009.

[11] P. Chang, A. Spitkovsky, and J. Arons. Long term evolution of magnetic turbulence in relativistic collisionless shocks: electron-positron plasmas. *Astrophys. J*, 674:378–387, 2008.

[12] F. Fiuza, R. A. Fonseca, J. Tonge, W. B. Mori, and L. O. Silva. Weibel-instability-mediated collisionless shocks in the laboratory with ultraintense lasers. *Phys. Rev. Lett.*, 108:235004, 2012.

[13] A. Gruzinov. Gamma-ray burst phenomenology, shock dynamo, and the first magnetic fields. *Astrophys. J.*, 563:L15–L18, 2001.

[14] U. Keshet, B. Katz, A. Spitkovsky, and E. Waxman. Magnetic field evolution in relativistic unmagnetized collisionless shocks. *Astrophys. J.*, 693:L127–L130, 2009.

[15] H. Zinnecker and Rayner J. T. McCaughrean, M. J. A symmetrically pulsed jet of gas from an invisible protostar in Orion. *Nature*, 394:862–865, 1998.

[16] Pedersen T.S. *The PAX/APEX experiment for production of a pair plasma.* Available at $http://www.ipp.mpg.de/3335368/pair_plasma$: Accessed 27/01/2016, 2016.

[17] P. Muggli, S. F. Martins, J. Vieira, and L. O. Silva. *Interaction of ultra relativistic e- e+ fireball beam.* Available at http://arxiv.org/abs/1306.4380, 2013.

[18] R. G. Greaves, M. D. Tinkle, and C. M. Surko. Creation and uses of positron plasmas. *Physics of Plasmas*, 1(5):1439–1446, 1994.

[19] H. Chen, S. C. Wilks, D. D. Meyerhofer, J. Bonlie, C. D. Chen, S. N. Chen, C. Courtois, L. Elberson, G. Gregori, W. Kruer, O. Landoas, J. Mithen, J. Myatt, C. D. Murphy, P. Nilson, D. Price, M. Schneider, R. Shepherd, C. Stoeckl, M. Tabak, R. Tommasini, and P. Beiersdorfer. Relativistic quasimonoenergetic positron jets from intense laser-solid interactions. *Phys. Rev. Lett.*, 105:015003, 2010.

[20] C. Gahn, G. D. Tsakiris, G. Pretzler, K. J. Witte, P. Thirolf, D. Habs, C. Delfin, and C.-G. Wahlstrm. Generation of mev electrons and positrons with femtosecond pulses from a table-top laser system. *Physics of Plasmas*, 9(3):987–999, 2002.

[21] G. Sarri, W. Schumaker, A. Di Piazza, M. Vargas, B. Dromey, M. E. Dieckmann, V. Chvykov, A. Maksimchuk, V. Yanovsky, Z. H. He, B. X. Hou, J. A. Nees,

A. G. R. Thomas, C. H. Keitel, M. Zepf, and K. Krushelnick. Table-top laser-based source of femtosecond, collimated, ultrarelativistic positron beams. *Phys. Rev. Lett.*, 110:255002, 2013.

[22] G. Sarri, K. Poder, J. Cole, W. Schumaker, A. Di Piazza, B. Reville, D. Doria, B. Dromey, L. Gizzi, A. Green, G. Grittani, S. Kar, C. H. Keitel, K. Krushelnick, S. Kushel, S. Mangles, Z. Najmudin, A. G. R. Thomas, M. Vargas, and M. Zepf. *Generation of a neutral, high-density electron-positron plasma in the laboratory.* Available at http://arxiv.org/abs/1312.0211, 2013.

[23] R. A. M. J. Wijers and T. J. Galama. Physical parameters of grb 970508 and grb 971214 from their afterglow synchrotron emission. *Astrophys. J.*, 523(1):177, 1999.

[24] T. J. Galama, M. S. Briggs, R. A. M. J. Wijers, P. M. Vreeswijk, E. Rol, D. Band, J. van Paradijs, C. Kouveliotou, R. D. Preece, M. Bremer, I. A. Smith, R. P. J. Tilanus, A. G. de Bruyn, R. G. Strom, G. Pooley, A. J. Castro-Tirado, N. Tanvir, C. Robinson, K. Hurley, J. Heise, J. Telting, R. G. M. Rutten, C. Packham, R. Swaters, J. K. Davies, A. Fassia, S. F. Green, M. J. Foster, R. Sagar, A. K. Pandey, Nilakshi, R. K. S. Yadav, E. O. Ofek, E. Leibowitz, P. Ibbetson, J. Rhoads, E. Falco, C. Petry, C Impey, T. R. Geballe, and D. Bhattacharya. The effect of magnetic fields on gamma-ray bursts inferred from multi-wavelength observations of the burst of 23 january 1999. *Nature*, 398:394–399, 1999.

[25] P. M. Vreeswijk, T. J. Galama, A. Owens, T. Oosterbroek, T. R. Geballe, J. van Paradijs, P. J. Groot, C. Kouveliotou, T. Koshut, N. Tanvir, R. A. M. J. Wijers, E. Pian, E. Palazzi, F. Frontera, N. Masetti, C. Robinson, M. Briggs, J. J. M. in t Zand, J. Heise, L. Piro, E. Costa, M. Feroci, L. A. Antonelli, K. Hurley, J. Greiner, D. A. Smith, A. M. Levine, Y. Lipkin, E. Leibowitz, C. Lidman, A. Pizzella, H. Bhnhardt, V. Doublier, S. Chaty, I. Smail, A. Blain, J. H. Hough, S. Young, and N. Suntzeff. The x-ray, optical, and infrared counterpart to grb 980703. *Astrophys. J.*, 523(1):171, 1999.

[26] E. Waxman. Gamma-ray bursts and collisionless shocks. *Plasma physics and controlled fusion*, 48(12B):B137, 2006.

[27] A. Gruzinov. Gamma-ray rurst phenomenology, shock dynamo, and the first magnetic fields. *Astrophys. J. Lett.*, 563(1):L15, 2001.

[28] M. Milosavljevi and E. Nakar. The cosmic-ray precursor of relativistic collisionless shocks: A missing link in gamma-ray burst afterglows. *Astrophys. J.*, 651(2):979, 2006.

[29] J. Vieira, K. Schoeffler, N. Shukla, and L.O. Silva. *Current filamentation instability of quasi-neutral fireball e-e+ beams*. Instituto Superior Tecnico, Lisbon, 2015.

[30] G. Sarri, C.A. Cecchetti, L. Romagnani, C.M. Brown, D.J. Hoarty, S. James, J. Morton, M.E. Dieckmann, R. Jung, O. Willi, S.V. Bulanov, F. Pegoraro, and M. Borghesi. Application of laser-driven proton beams to the radiography of intense laser-hohlraum interactions. *New J. Phys.*, 12:045006–045006–12, 2010.

[31] G. Sarri. *Private communication*. 2015-2016.

[32] G. Sarri, W. Schumaker, A. Di Piazza, K. Poder, J. M. Cole, M. Vargas, D. Doria, S. Kushel, B. Dromey, G. Grittani, L. Gizzi, M. E. Dieckmann, A. Green, V. Chvykov, A. Maksimchuk, V. Yanovsky, Z. H. He, B. X. Hou, J. A. Nees, S. Kar, Z. Najmudin, A. G. R. Thomas, C. H. Keitel, K. Krushelnick, and M. Zepf. Laser-driven generation of collimated ultra-relativistic positron beams. *Plasma Phys. Control. Fusion*, 55(12):124017, 2013.

[33] T. Eichner, F. Grüner, S. Becker, M. Fuchs, D. Habs, R. Weingartner, U. Schramm, H. Backe, P. Kunz, and W. Lauth. Miniature magnetic devices for laser-based, table-top free-electron lasers. *Phys. Rev. ST Accel. Beams*, 10:082401, 2007.

[34] H. Wollnik. *Optics of Charged Particles*. Oval Rd, London: Academic Press, 1987.

[35] Inc. (SIS) Scientific Instrument Services. *Simion*. Available at *http* : *//simion.com/*: Accessed 16/02/2016, 2015.

5 Acknowledgements

I would like to thank my supervisor Dr. G. Sarri for all his guidance and encouragement throughout this thesis. I would also like to thank Prof. J. Greenwood for his help with setting up the Simion simulations. To Cormac Hyland and David Waide for their help and guidance with MATLAB. And lastly to my fiance Alex for all her continuing love, support and encouragement.

A MATLAB Code

Below is a section of code written in matlab to calculate the thin lens approximation parameters of a quadrupole triplet system.

```
%Constants
E = 600;
e = 1.602176620e-19;
u = 1.660539040e-27;
m_0 = 5.48579909070e-04;
eta = E/(1862.9882*m_0);
m_r = m_0*(1+(2*eta));
m_r = m_r*u;
v = 13.891*(sqrt((E*(1+eta))/m_0))/(1+2*eta);
v = v*1e6;

%Variables
G = 0.003;
B1 = 1.1;
B2 = 1.2;
B3 = 1.2;
w1 = 0.02;
w2 = 0.05;
w3 = 0.05;
%d1 = 0.115;
d2 = 0.05;
%d = 0.10;
%Key Formulas
k1 = (B1*e)/(G*m_r*v);
k2 = (B2*e)/(G*m_r*v);
```

```
k3 = (B3*e)/(G*m_r*v);
f1x = 1/-(k1*w1);   %change of sign when in the y direction, since...
                    %focusing lens becomes a defocusing lens.
f2x = 1/(k2*w2);  % "
f3x = 1/-(k3*w3);   % "
f1y = 1/(k1*w1);
f2y = 1/-(k2*w2);
f3y = 1/(k3*w3);
dbar1 = d1+((w1+w2)/2);
dbar2 = d2+((w2+w3)/2);
Msx = [1,0;-1/f3x,1]*[1,dbar2;0,1]*[1,0;-1/f2x,1]*[1,dbar1;0,1]*...
    [1,0;-1/f1x,1];
Msy = [1,0;-1/f3y,1]*[1,dbar2;0,1]*[1,0;-1/f2y,1]*[1,dbar1;0,1]*...
    [1,0;-1/f1y,1];
lbar1x = (-4-Msx(2,2))/Msx(2,1);
lbar1y = (-4-Msy(2,2))/Msy(2,1);
lbar2x = (((-Msx(1,1))*lbar1x)-(Msx(1,2)))/((Msx(2,2))+((Msx(2,1))...
    *lbar1x));
lbar2y = (((-Msy(1,1))*lbar1y)-(Msy(1,2)))/((Msy(2,2))+((Msy(2,1))...
    *lbar1y));
overallx = lbar1x+dbar1+dbar2+lbar2x;
overally = lbar1y+dbar1+dbar2+lbar2y;
y1x = lbar1x*tan(0.0025);
y1y = lbar1y*tan(0.0025);
y2x = lbar2x*tan(0.010);
y2y = lbar2y*tan(0.010);
maxx = 2*(lbar1x+dbar1-((dbar1*lbar1x)/f1x))*tan(0.0025);
maxy = 2*(lbar1y+dbar1-((dbar1*lbar1y)/f1y))*tan(0.0025);

%Printing to screen
output=[lbar1x, lbar1y];
fprintf (['d1 = %d m  lbar1x = %d m  lbar2x = %d m  overallx = %d m'
   ... 'maxx = %d m \n'],d1,lbar1x,lbar2x,overallx,maxx);
fprintf (['d1 = %d m  lbar1y = %d m  lbar2y = %d m  overally = %d m'
   ... 'maxy = %d m \n'],d1,lbar1y,lbar2y,overally,maxy);
```

This next section of code iterates through a parameter (in this case d_1) for a set number of steps, each time putting it into the last section of code and calculating the output value.

```
1
2  %% Define matrices to plot
3  a_mat=NaN(100,1);
4  b_mat=NaN(100,1);
5  % c_mat=zeros(10,1);
6  x_axis=NaN(100,1);
7
8  %% Section 2
9  for n = 10:1:700
10     d1=n/1000;              % Change B3 (the x_axis)
11     Level4_Project;           % Run the project script (with B3 defined
12                             ...  %previous line)
13     a_mat(n)=output(1);       % Take first value from matrix "output" -
14                              ... %defined at end of project script
15     b_mat(n)=output(2);       % Take 2nd value    "   "   "   "
16     % c_mat(n)=output(3);       % " "   "   "   "
17     x_axis(n)=d1;             % Assign values to x-axis
18 end
19 % figure % Plots one figure at a time
20 hold on  % Makes plots on top of each other
21 plot(x_axis,a_mat,'red')
22 plot(x_axis,b_mat,'blue')
23 %plot(x_axis,c_mat)
24 xlabel('d1 / m','FontSize', 18)
25 ylabel('lbar1 / m','FontSize', 18)
26 title(['Source Length (Lbar1) as a Function of Distance (d1) Between'
27    ... 'Quadrupoles'],'FontSize', 18)
28 legend('Lbar1x','Lbar1y')
29 %[x,y]=ginput(n);
30 %[x,y]=ginput;
31 %[x,y,button]=ginput(1)
```